Disruption Mitigation Efficiency and Scaling with Thermal Energy Fraction on ASDEX Upgrade

U. A. Sheikh[1], P. David[2], O. Ficker[3], M. Bernert[2], D. Brida[2], M. Dibon[2], B. Duval[1], M. Faitsch[2], M. Maraschek[2], G. Papp[2], G. Pautasso[2], C. Sozzi[4], the AUG team[5] and EUROfusion MST1 team[6]

[1] École Polytechnique Fédérale de Lausanne (EPFL), Swiss Plasma Center (SPC), CH-1015 Lausanne, Switzerland

[2] Max Planck Institute für Plasmaphysik, Garching, Germany

[3] Institute of Plasma Physics AS CR, Za Slovankou 1782/3, 182 00 Praha 8, Czech Republic

[4] Istituto di Fisica del Plasma - Universita degli Studi di Milano-Bicocca, Milan, Italy

[5] See the author list Meyer, H. et al. Nucl. Fusion 59 (2019) 112014

[6] See the author list Labit, B. *et al* Nucl. Fusion 59 (2019) 086020

E-mail: `umar.sheikh@epfl.ch`

August 2020

Abstract. Disruption mitigation remains a critical and unresolved issue for ITER. Measurement uncertainties preventing quantification of a system's efficacy remains a significant hurdle in producing and validating a viable disruption mitigation system. This study addresses this issue through the creation of a dataset on the ASDEX Upgrade tokamak targeted at developing analysis techniques to quantify mitigation that are applicable irrespective of the disruption mitigation system being studied. These experiments used a range of thermal energy fractions to address concerns for ITER from JET massive gas injection (MGI) experiments showing a decrease in efficacy with increasing thermal energy fraction. The dataset produced in this study used MGI valves in two toroidal locations. The high resolution foil bolometers and AXUV diode arrays were used to infer radiation emission profiles at varying toroidal distances from the injection location. The fueling efficiency of the two systems was found to be comparable and toroidal asymmetries over the entire disruption were found to be negligible. The AXUV diodes were cross-calibrated with the foil bolometers and used to estimate the thermal energy radiated and magnetic energy coupled to the vessel structure and coils. It was estimated that 75-95% of the thermal energy was radiated and an almost constant 60% of the total magnetic energy was coupled. Radiated energy fractions of 0.8-1.0 were calculated and no decrease as a function of thermal energy fraction was found. A $\pm 20\%$ variation in the coupled magnetic energy was explored and it did not alter this trend.

Keywords: Disruption mitigation, power balance, bolometers

1. Introduction

Disruptions have the potential to release large amounts of thermal and magnetic energy (W_{th} and W_{mag}) in millisecond time-scales and this can result in extreme heat loads on plasma facing components and electromagnetic (EM) forces on the vessel [1]. Existing machines are capable of handling these forces and loads as they were designed to study the disruptive boundaries of tokamak operation. It is not technically feasible to allow unmitigated disruptions at the high stored energies on ITER as the predicted heat load would evaporate up to $100\,\mu$m of the divertor target plate [2]. The last line of defence to prevent such an outcome is a disruption mitigation system. The most common approach is injection of a massive amount of material relative to the plasma mass. The goal of such a system is threefold:

- Radiation of W_{th} before it can be deposited on the targets
- Mitigation of EM loads
- Prevention or mitigation of high current "runaway" electron beams

Specifically, the ITER mitigation system needs to be able to reduce vessel forces by a factor of 2-3 and the thermal loads by at least 90% to ensure the integrity and lifetime of the machine [3, 4]. Runaway electrons (RE) are of particular concern on ITER as they are expected to exceed $10\,$MA [1]. Relatively low RE currents of $0.5\,$MA on JET have caused average temperature increases of up to $700°\,$C on the upper dump plate and concentrated localised damage on impact with a wall [1, 5]. Thus a RE current of $10\,$MA would cause severe melting of plasma facing components on ITER and must be avoided. As of yet, no technique has been proven to reliably achieve these targets for a range of plasma scenarios.

Two main systems for massive material injection have been extensively studied; massive gas injection (MGI) and shattered pellet injection (SPI). MGI has been explored on a range of tokamaks including Alcator C-mod, ASDEX Upgrade (AUG), DIII-D, JT60-U, MAST, TEXTOR, Tore Supra, J-TEXT and HL-2A [6, 7, 8, 9, 10, 11, 12]. SPI on the other hand is relatively new and has only been studied in detail on DIII-D with further, more recent experiments on JET, K-STAR, J-TEXT and HL-2A [13, 14, 15, 16, 17]. MGI and SPI systems have reported over 90% of the initial W_{mag} as being radiated [18, 19], however the scatter on total radiated energy (W_{rad}) is large depending on machine parameters as shown in Figure 1 [20].

A particularly worrying trend observed on JET has been the decrease in radiated energy fraction (f_{rad}) with increasing stored thermal energy fraction (f_{th}), as shown in Figure 2 [20, 21, 22]. The definition used in this study for the two parameters is outlined in Equations 1 and 2. W_{th} denotes the stored thermal energy, W_{mag} the stored magnetic energy and W_{coupled} the magnetic energy dissipated in the surrounding structure (vessel and coils) during the current quench (CQ). This has been calculated for the dataset presented in Figure 2 using the circuit model, similar to that described in Lehnen 2013 [23]. The W_{rad} presented has been inferred using the horizontal foil bolometer
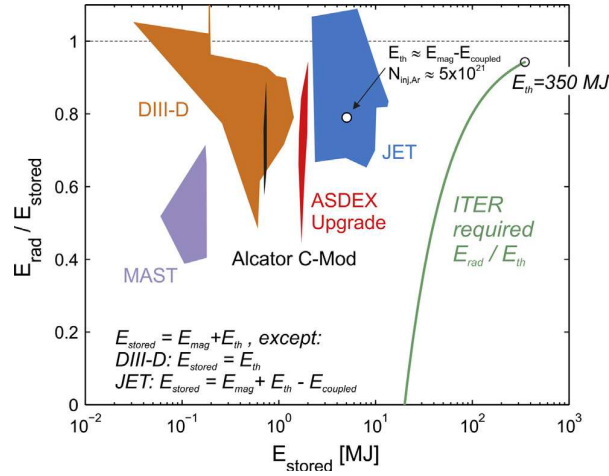
Figure 1. MGI efficiency using high-Z noble gases (neon, argon) and mixtures of these with D_2 and He. The white JET data point indicates the maximum achievable radiated energy fraction at high thermal energy fraction on JET [20].

array and integrated across the entire disruption. This trend is extremely concerning as ITER is targeting to operate close to an f_{th} of 0.6 during high performance discharges.

$$f_{rad} = W_{rad}/(W_{mag} + W_{th} - W_{coupled}) \tag{1}$$

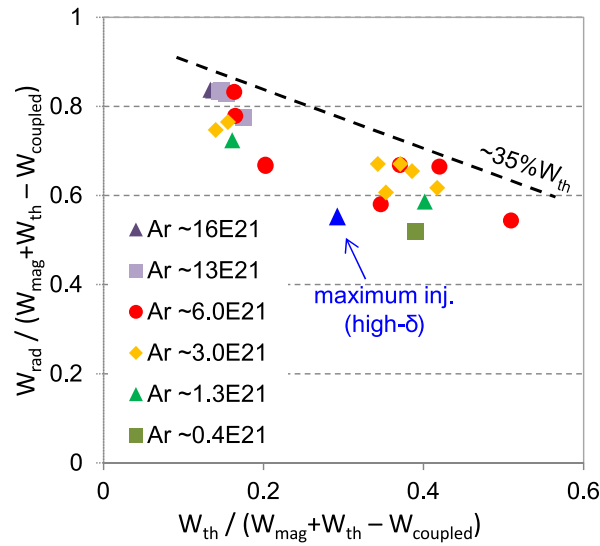$$f_{th} = W_{th}/(W_{mag} + W_{th} - W_{coupled}) \tag{2}$$

Figure 2. Reduction of f_{rad} with increasing f_{th} observed with JET MGI [21].

The inferred mitigation efficiency for similar discharges can have large variations and uncertainties as measurements using the standard set of diagnostics for W_{rad} and heat fluxes on plasma facing components can be severely hampered during a mitigated disruption. For example, foil bolometers that are used to measure absolute radiated

power operate on time scales too slow to infer W_{rad} before the thermal quench (TQ). AXUV diodes are fast enough to separate the TQ and CQ but if they are slightly aged, their sensitivity can vary as a function of wavelength. However, it has been shown that the diode response does settle after roughly 300 seconds of plasma operation [24]. This makes the diodes unsuitable for direct absolute measurements of W_{rad}. Heat flux measurements using infra-red cameras can be difficult due to IR emission from the injected gas and reflections from the vessel structure producing background signal and artefacts that taint the calibration. Experiments on carbon wall machines such as DIII-D have been able to use post disruption tile temperatures to infer information about the heat loads. This was possible due to the lower thermal conductivity of carbon resulting in a hotter tile surface for a longer period of time after the disruption. Such an approach is more difficult on metal wall machines due to higher thermal conductivity, lower emissivity and higher reflectivity [25].

These diagnostic challenges result in an uncertainty that is larger than the mitigation efficiency criteria. Without a reduction in these uncertainties it is currently not possible to ensure a mitigation system can meet requirements on a larger machine such as ITER. To this end, the goals of this study are to experimentally investigate the reduction in f_{rad} with increasing f_{th} on AUG, investigate the impact of inferred W_{rad} as a function of toroidal distance between injection and measurement location and estimate the uncertainties in the energy balance methodology. It is envisioned that the diagnostic analysis developed in this study be applicable independent of the material injection system being employed.

2. Experiment Description and Diagnostics

AUG is a D shaped full metal wall machine with a major radius of 1.65 m and field and plasma current of up to 3.2 T and 1.4 MA respectively [26]. The auxiliary heating systems are capable of providing up to 20 MW of neutral beam heating (NBH), 7 MW of ion cyclotron heating (ICRH) and 6 MW of electron cyclotron heating (ECRH) split between 140 GHz and 105 GHz [27]. AUG is uniquely equipped with MGI systems in several toroidal and poloidal locations as well as a large range of relevant diagnostics including a full array of foil bolometers in a single toroidal location, AXUV diode arrays in two toroidal locations, infra-red (IR) cameras, fast CO2 interferometers and strain gauges on the vessel support structure [28].

Figure 3c illustrates the toroidal positions of the primary diagnostics and gas injection systems used in this study. The blue rectangles represent the three IR cameras that were used in this study and their relative viewing location. These were arranged to provide a wide view of the overall divertor, two tiles on the outer target optimised for IR measurements and an optimised "strip" on the outer target. The electromagnetic (EM) loads were monitored using strain gauges on the support columns of the tokamak and shunt resistors in the divertor to estimate Halo currents (I_{halo}).
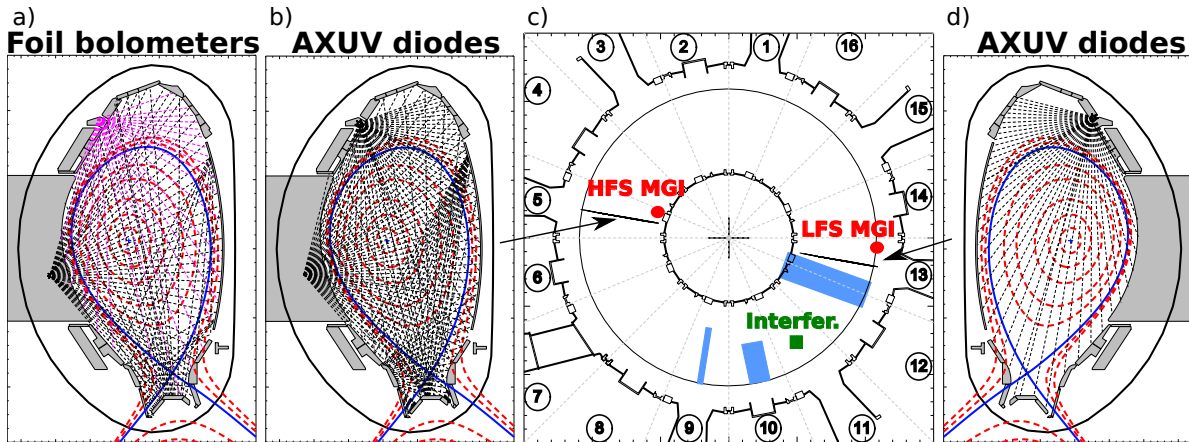
Figure 3. Poloidal lines of sight of the foil bolometers (a), AXUV diodes in sector 5 (b) and in sector 13 (d) and their relative toroidal locations (c). Blue rectangles - locations and approximate viewing regions of the IR cameras. Red circles - locations of the two MGI systems. Green rectangle - vertical line of sight of the CO2 interferometer.

2.1. Massive Gas Injection Systems

The MGI valves used in this study were in-vessel on the low field side (LFS) and high field side (HFS) in sectors 13 and 5 respectively. Both valves are capable of opening in approximately 1 ms and withstanding the demanding in-vessel environment. They operate using a pneumatic piston driven by compressed air, pairs of piezoelectric-actuators and a disk spring that opens the valves as outlined in Pautasso 2008 and 2015 [28, 29].

The MGI systems were operated with a mixture of 90% deuterium and 10% neon or argon. The maximum allowed quantity limited by deuterium use regulations, was used for the "large" injection discharges with $\sim 1.7 \cdot 10^{22}$ particles injected. "Small" injections of $\sim 0.9 \cdot 10^{22}$ particles were also performed to investigate whether $f_{\rm rad}$ had saturated to have a direct comparison with JET results.

2.2. Radiation Diagnostics

Foil bolometers and AXUV diodes are used during standard operation on AUG over a range of poloidal locations to achieve full coverage in sector 5. An additional AXUV camera on the upper LFS is also available in sector 13 providing a single "fan" of chords across the machine. The operation of these diagnostics and the analysis techniques compared are briefly introduced in the following subsections.

2.2.1. Foil Bolometers

Foil bolometers provide absolute radiation measurements due to their flat spectral response from approximately 50 eV to the keV range [30]. The temporal resolution during standard operation is 30 ms and is a result of their thermal inertia as they operate, essentially, as thermistor thermometers. The high radiative power achieved

with MGI in this study resulted in higher heat fluxes on the foils, producing larger bridge voltages, allowing a reduction in the temporal averaging window to $400\,\mu$s whilst maintaining signal to noise ratios comparable to standard operation.

The bolometery system on AUG consists of 112 lines from 6 cameras as shown in Figure 3a. All six cameras were analysed with two tomographic inversion techniques to provide radiated power as a function of time. The standard tomographic inversion technique on AUG allows spatial smoothing along flux surfaces (Flux Surface Smoothing - FSS) and does not reject negative values [31]. The drawback of this approach is a valid equilibrium reconstruction is required and this is often challenging during a disruption. The second inversion technique requires no equilibrium information, instead resolving the power density on a rectangular grid after smoothing the experimental data in the R and z directions [32]. This technique does not permit negative power values. These two techniques will be referred to as "FSS" and "no FSS" respectively.

A third radiated power inference technique was applied using a single camera indicated using magenta lines of sight in Figure 3a. Here, constant radiation along flux surfaces is assumed and does not produce inverted images [33]. This method provides a direct comparison with JET measurements, which uses only a single camera. This technique will be referred to as "single camera" for this study.

2.2.2. AXUV Diode Arrays

AXUV diodes are silicon based detectors that are only sensitive to incoming photons with a response that is a function of photon energy. This sensitivity variation can be exacerbated over time by damage from high energy photons resulting in significantly reduced sensitivity in the ultra-violet (UV) spectral range, as shown in Figure 4 [24]. Whilst it has been shown that their response stabilises after a given exposure time, they cannot be used directly for absolute measurements of radiated power. Their advantage is a high temporal resolution (up to $500\,$kHz on AUG) allowing qualitative studies of fast transient events such as disruption mitigation.
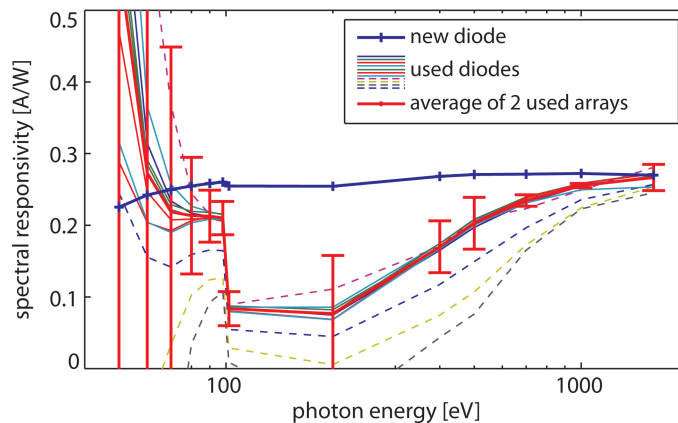

Figure 4. Spectral response of new and used AXUV diodes measured in a synchrotron [24]

Table 1. Nominal plasma parameters used and heating employed for the high and low f_{th} scenarios.

I_{p}=0.8 MA	$B_{\mathrm{T}} = 2.5$ T	q_{95} 4.9
κ=1.72	δ_{o}=0.11	δ_{u}=0.50
High W_{th} Scenario	7.5 MW NBH	3.5 MW ECRH
Low W_{th} Scenario	2.5 MW NBH	1.8 MW ECRH

The AXUV system on AUG consists of 176 lines of sight in sector 5 as shown by the black lines in Figure 3b and foil bolometers in the same sector allow for cross-calibration. An additional single camera system with 32 lines of sight is available in sector 13, as shown in Figure 3d. Inversions using Pytomo [34] were performed for both systems independently allowing a qualitative comparison of radiation asymmetries. This inversion technique allows FSS and negative emission values.

2.3. Scenario Description

AUG was operated well below its performance limits to ensure machine safety during potentially poorly mitigated discharges. A single scenario was selected for the whole study with approximately 1 MJ of W_{mag}. Auxiliary heating was varied to provide a scan in W_{th} and consequently f_{th}. The scenario parameters with the heating schemes for "high" and "low" W_{th} are provided in Table 1. Each reported discharge terminated following MGI injection into a healthy plasma at 3.000 s for LFS injection and 3.035 s for HFS injection.

Figure 5 provides an overview of a reference high power discharge (#35653) mitigated with the LFS valve in sector 13. The vertical lines indicate the nominal sequence of events; valve opening (red), gas arrival at plasma edge (green), start of the TQ (black) and start of CQ(magenta). The arrival of the gas at the plasma edge is inferred from the AXUV diodes in the injection sector. The time between gas arrival and the start of the TQ will be referred to as the pre-TQ time. The sharp drop in core soft x-ray (SXR) emission indicates the loss of W_{th} during the TQ and the slight preceding increase in plasma current marks the beginning of the CQ.

3. Results

A dataset comprising of 11 discharges mitigated using the sector 13 LFS valve and 6 discharges mitigated using the sector 5 HFS valve were produced for this study. The following sections present analyses of MGI injection and assimilation, radiated energy and the mitigation of thermal and magnetic energy. The energy loss channels are then combined to generate an energy balance and compute f_{rad}.
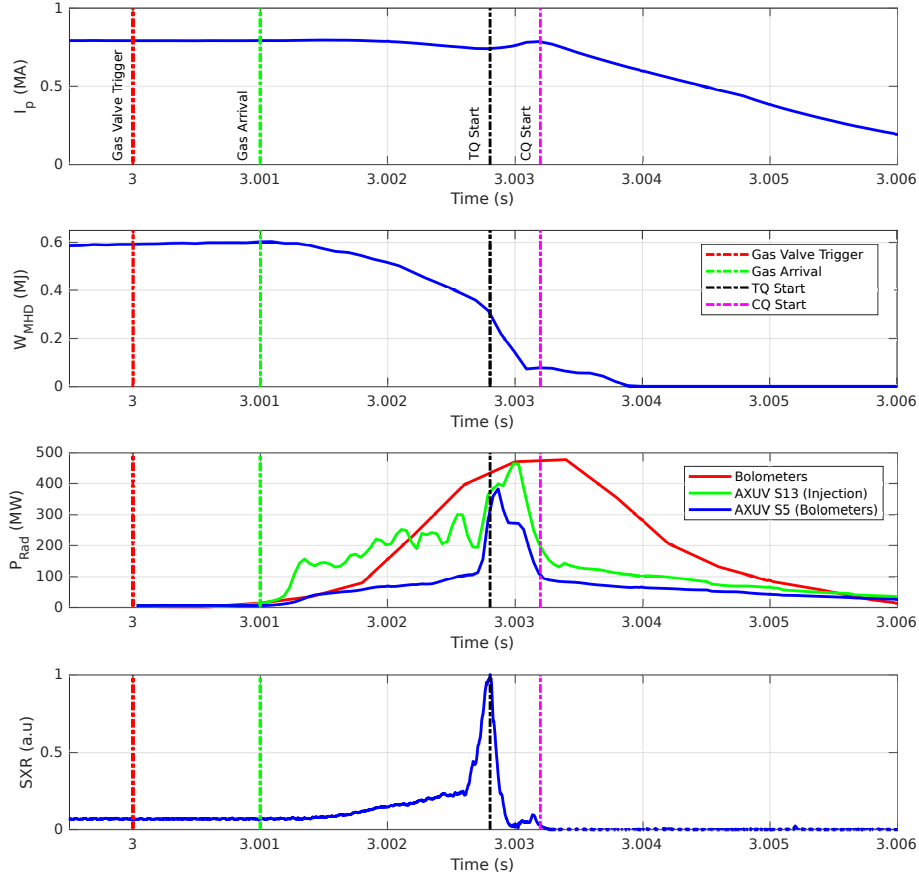
Figure 5. Nominal discharge plasma current, W_{th}, radiated power and core SXR emission from top to bottom. Dashed lines mark valve opening, gas arrival, TQ start and CQ start from left to right.

3.1. MGI Injection and Assimilation

The response time of the MGI valves can be estimated from the flight time of the injected gas; the delay between trigger time of the MGI and a doubling of the AXUV diodes signal in the injection sector. Figure 6 left presents the flight time for both valves using 10% argon and neon mixtures and two injection quantities. The number of injected particles was controlled by the pressure in the MGI reservoir. This required a lower gas pressure for the larger reservoir of the HFS valve to match the total number of particles injected. The flight time using the HFS valve was shorter than for the LFS valve due to valve position relative to the diodes. The neon mixture reached the plasma in less than one ms from the HFS valve and as expected, the argon mixture took longer.

The pre-TQ time as a function of injected particles is presented in Figure 6 right and it does not appear to be a function of gas mixture but does vary with valve location. Injections from the LFS valve, shown by empty symbols, appear to have an almost constant pre-TQ time of 1.5-1.8 ms, whereas injections from the HFS valve have approximately double the pre-TQ time. This is attributed to two factors: a delay in detecting gas arrival for the LFS valve and a relatively lower reservoir pressure (due
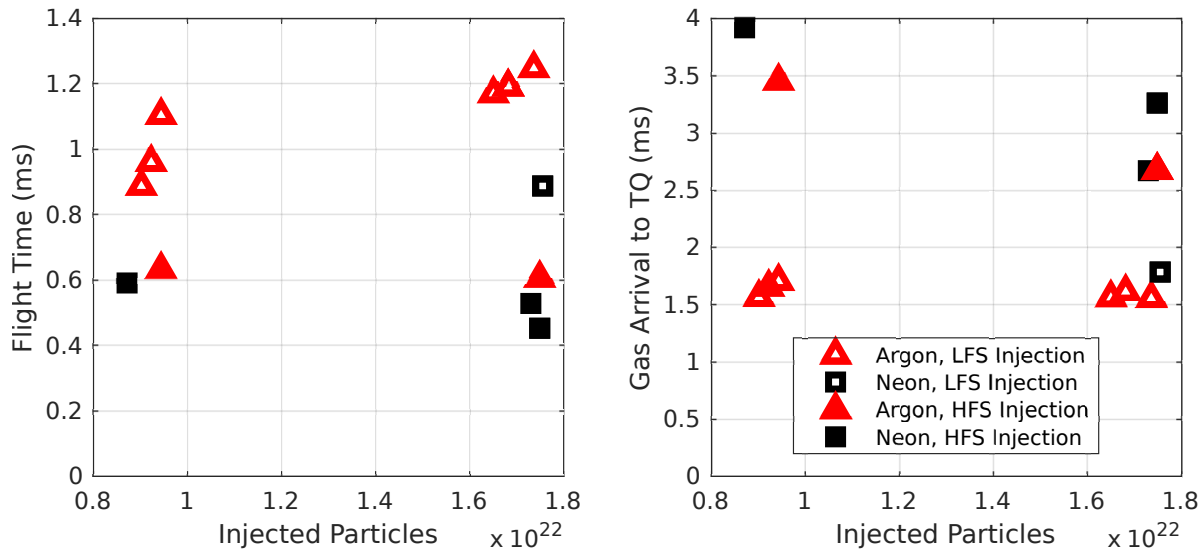
Figure 6. Flight time of particles (left) and pre-TQ time of each discharge as a function of number of particles injected (right).

to a larger volume) producing a lower flow rate for the HFS.

The quantity of gas assimilated with "large" injections could not be estimated from density measurements that were corrupted by numerous fringe jumps. The smaller injections produced fewer fringe jumps and density traces for two representative neon injections into high W_{th} discharges are presented in Figure 7. An earlier increase in density is observed for LFS injection ascribed to its toroidal proximity to the interferometer. The sudden changes in density observed for LFS injection (green) at $3.003\,\text{s}$ and $3.005\,\text{s}$ show examples of fringe jumps. Accounting for the fringe jumps, the increase in density measured for LFS and HFS injection is within 10%. The decreasing value of density at $3.006\,\text{s}$ observed with HFS injection may be due to measurement error but this cannot be confirmed and it does not impact the findings. The density trace during the CQ was measured to be almost identical between the two valves. This indicates that both have similar fueling efficiency with the same number of particles assimilated.

Previous studies reported the HFS valve has relatively higher fueling efficiency at low injection amounts [28]. As the injected quantity was increased, saturation was achieved and both valves produced similar plasma density increases. The measurements presented in this work find almost equal assimilation from both valves for the "small" injection quantity. Although termed "small" in this report, the injection is over $10\times$ the plasma inventory ($\sim 8.4 \cdot 10^{20}$). Fast interferometry measurements indicate a factor of 6 increase in density, indicating $\sim 4 \cdot 10^{21}$ particles of the $\sim 9 \cdot 10^{21}$ injected were assimilated with both valves. Furthermore, this study was conducted with different discharge parameters, such as lower plasma current, and different injection gas mixtures (90% deuterium mixtures in this study compared to pure neon in Pautasso 2015 [28]). It is therefore assumed that comparable fueling efficiency has already been achieved for the
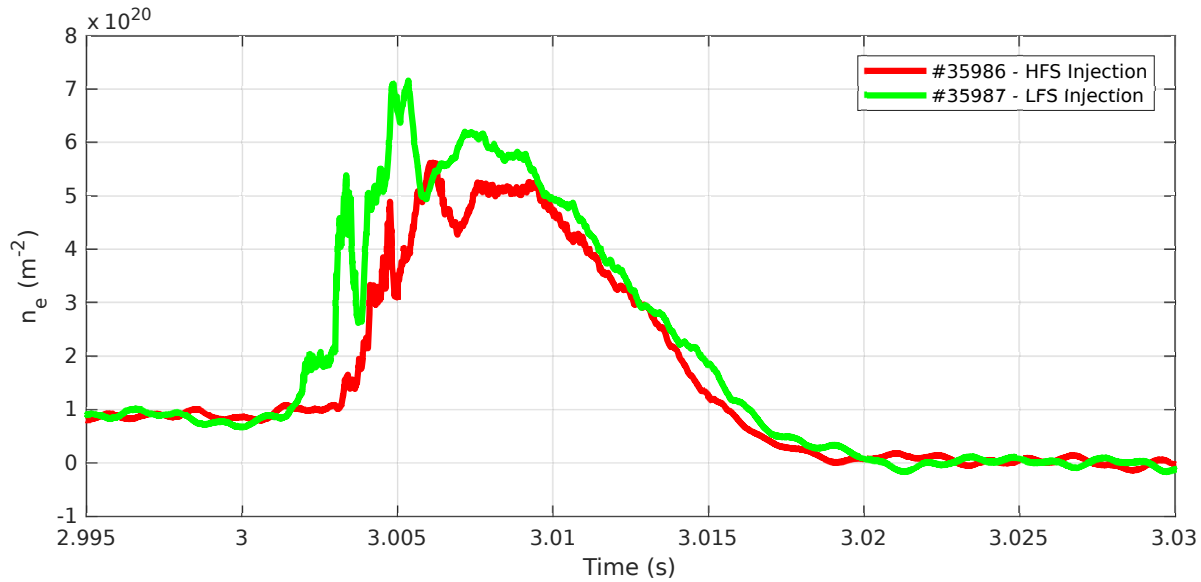
Figure 7. Density traces from the CO2 interferometer for "small" neon injections into high W_{th} discharges with the HFS (red) and LFS (green) valves. The HFS injection has been shifted in time to match.

lower injection quantity that will remain comparable for the higher injection quantities.

The CQ time (τ_{CQ}), linearly extrapolated from the 80%-20% CQ time, can be used to approximate the relative assimilation of impurities into the plasma. This is possible as τ_{CQ} is a function of plasma resistivity and self-inductance, assuming the plasma shape does not change significantly and there are no large vertical displacements [28]. Thus, a similar τ_{CQ} for a given impurity would indicate a similar assimilated amount. Figure 8 presents τ_{CQ} as a function of the average atomic number of the gas mixture (Mix. Z) and the number of injected particles. Both valves produced similar τ_{CQ} for a given number of injected particles and Mix. Z, indicating the same assimilation efficiency for both valves for each gas. Saturation of τ_{CQ} is not achieved for the smaller injection amount and as expected, a shorter τ_{CQ} is measured for argon. Doubling the quantity of argon injected produced only a $\sim$15% decrease in τ_{CQ}. Doubling the quantity of injected neon reduced τ_{CQ} by $\sim$75% in line with values comparable with large argon injection indicating saturation of assimilated particles has been achieved.

3.2. Radiated Energy

The AXUV diodes and bolometers were used to investigate radiation emission location, toroidal asymmetries and total radiated energy. The high temporal resolution of the AXUV diodes permits qualitative measurements of radiation emission location, impurity transport (poloidal and toroidal) and penetration depth. Figure 9 presents the temporal evolution of incident radiated power (on a logarithmic scale) per channel (diode) for the reference discharge. The three cameras presented are the DVC13 fan in sector 13 and the upper and lower LFS cameras in sector 5.
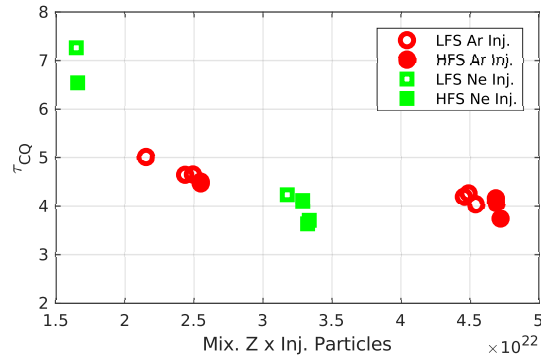
Figure 8. CQ time as a function of average atomic number of the gas mixture and the injected particles.
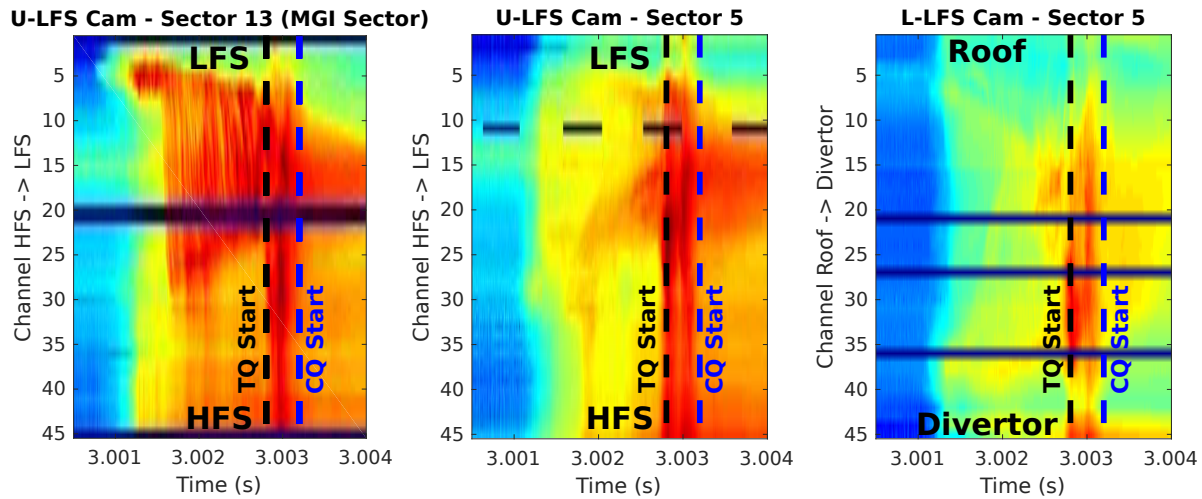

Figure 9. Temporal evolution of radiated power (on a logarithmic scale) per channel for the reference discharge (#35653). Left - DVC13 fan in sector 13, middle - the upper LFS cameras in sector 5, right - lower LFS camera in sector 5.

The emission from gas arrival at the LFS plasma edge is apparent from LFS injection on the AXUV camera in sector 13. The radiation is initially localised on the LFS and then produces a circulating pattern between the LFS and mid-plane until the TQ. This pattern is due to parallel impurity transport along helical field lines. An increase in radiation is measured in the opposite sector within $0.1\,\mathrm{ms}$ of gas arrival due to fast parallel transport of impurities. The relatively lower emission measured in the opposite sector is attributed to changes in the emission spectrum resulting in a relatively weaker response from the AXUV diodes that display strong spectral sensitivity behaviour.

The temporal evolution of radiated power for the three bolometer inference techniques and the AXUV diodes from both sectors are presented in Figure 10 for the reference discharge with LFS injection (#35653) and a comparable discharge with HFS injection (#35982). The AXUV diode signals have been scaled by a factor of 25 to match the radiated power from the bolometers. A scaling factor of 15 in W_{rad} was observed

during flat-top operation, so a factor of 25 during a disruption is not implausible [35]. The difference in temporal resolution between the two diagnostics is apparent from the sharp changes in radiated power inferred from the diodes. For LFS injection, the diodes in sector 13 measured an early increase in radiated power in the injection sector (13) and larger total radiated energy across the disruption relative to the diode measurements in sector 5. This is attributed to a relatively high spectral response of the diodes to visible photons (see Figure 4) and an analysis of toroidal asymmetries is presented in the following subsection. Measurements in sector 13 were not available during HFS injection discharges.
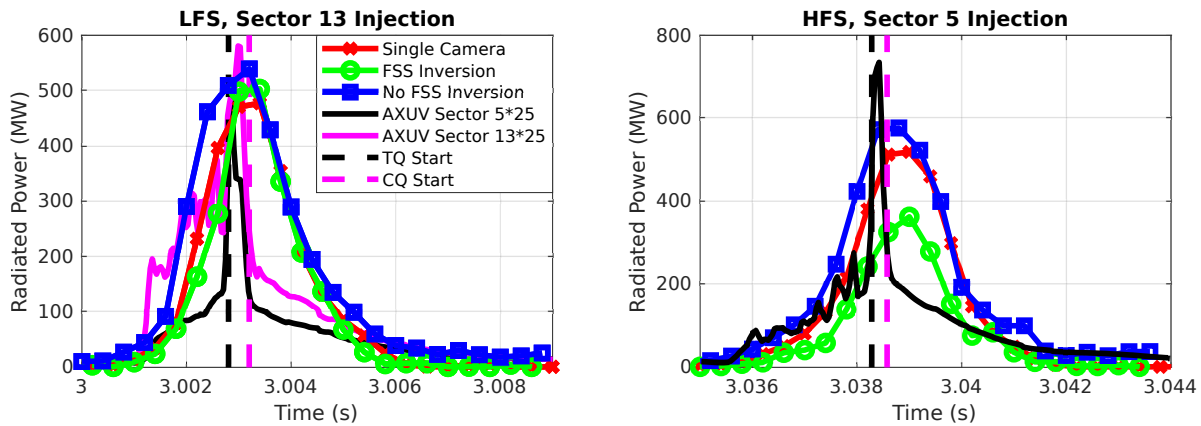

Figure 10. Radiated power from the three bolometer inference techniques and scaled AXUV diodes for LFS (left) and HFS (right) injection into comparable discharges (#35653 and #35982 respectively).

The bolometers measured a slower increase in radiated power over 2 ms by all three techniques with the inferred peak radiated powers are within 10% of each other for LFS injection. The no FSS inversion predicts the highest radiation in the pre-TQ phase and this was observed in all discharges. The source of this difference is attributed to variations in location of strong emission regions. The emission location during the CQ is expected to be more homogeneous and this is reflected by the comparable powers inferred after the TQ for LFS injection. The post TQ variation in radiated power for HFS injection is attributed to continued MGI injection from unempty reservoirs [28]. This results in localised radiation at the HFS and differences in inferred radiated power depending on the emission location calculated. The variation in inferred radiated power for localised and homogeneous plasma emission profiles illustrates the potential errors that can arise when using inversion codes benchmarked for standard operation during disruptions.

The sector 5 HFS injections are more challenging for the inversion algorithms as the radiation measurement is in the same sector, leading to strongly localised emission. The inverted profiles at peak power for the reference LFS and HFS injection discharges are presented in Figure 11. All four inversions place the bulk of radiation close to the HFS mid-plane and indicate significant radiation at the outer divertor. This implies that the

impurities have not penetrated to the core at this time but have been transported along flux surfaces from the injection location. The streaks of high or zero emission across the inverted image with the no FSS technique are inversion artefacts and suggest weaker regularisation.
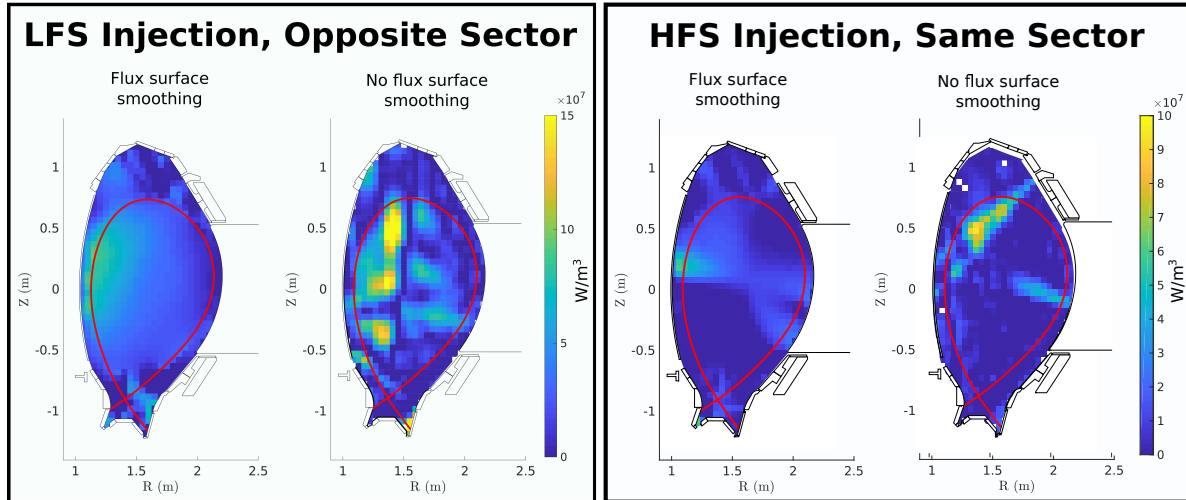

Figure 11. Tomographic inversions of bolometer data at peak radiation using the FSS method and the no FSS method for LFS (left) and HFS (right) injection into comparable discharges (#35653 and #35982 respectively).

The shapes of high radiating regions provide an insight into the influence of numerical smoothing along flux surfaces or R-z co-ordinates. An example of this is the smoothing along the HFS separatrix in the FSS inversion compared to strongly radiating regions in an almost vertical line across flux surfaces with the no FSS inversion for LFS injection. Stronger smoothing for the FSS inversion is able to better mask inversion artefacts from channels measuring increased localised radiation, which appear as streaks in the no FSS inversion. The disadvantage of strong smoothing is the reduction in spatial precision and radiation pattern localisation such as that observed in the outer divertor with the no FSS inversion.

The consistently higher radiated power computed with the no FSS inversion is attributed to the emission location being placed further inside the plasma at a larger radius. Consequently, a larger radiating volume is calculated and leads to a higher radiated power. Similarly, the single camera technique is expected to overestimate the radiated power as it assumes constant radiation emission along a flux surface, which leads to the localised radiation at the HFS being averaged across the entire flux surface. The impact of these factors on uncertainty in radiated power is discussed in Section 3.2.2.

Figure 12 presents the total W_{rad} integrated between the arrival of gas and the end of the CQ. The ratio between the inversion techniques varied from 1.2 to 2 in the LFS MGI mitigated discharges, with the single camera inferred W_{rad} fluctuating between the values from the inversions. The no FSS technique consistently predicted the highest

W_{rad}, whereas the FSS inversion consistently predicts the lowest. This result highlights the large variation possible in W_{rad} based on the inversion method applied and the need for further development of inversion methods.
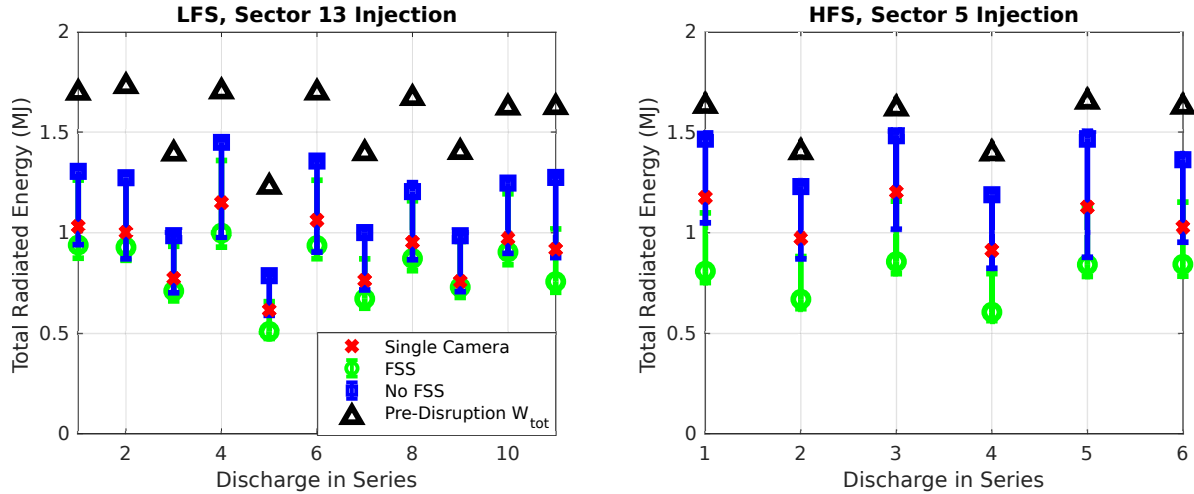

Figure 12. Total radiated energy for LFS MGI discharges (left) and HFS MGI discharges for the three bolometer inference techniques.

The ratio between the calculated radiated energies is approximately constant when using the HFS valve, which is in the same sector as the bolometers. The consistently higher W_{rad} from the no FSS technique is attributed to localisation of emission at larger radius and poorer convergence of the inversion. This is also demonstrated by the error bars (detailed in Section 3.2.2). The absolute values of W_{rad} with the no FSS inversion are over 90% of the total pre-disruption energy $(W_{\mathrm{th}} + W_{\mathrm{mag}})$, implying less than 10% of the total energy was deposited on the divertor and coupled to the structure during the CQ. This is unrealistically low based on the previously estimated 30% of W_{mag} coupling to the vessel structure and coils on AUG, 20-60% on JET and 50% on DIII-D [28, 36]. Based on the unrealistically high W_{rad} inferred, the no FSS inversion will not be used in the energy balance.

3.2.1. Radiation Asymmetries

The assumption of toroidal symmetry cannot always be applied in mitigated plasmas due to injection at a single toroidal location. The level of toroidal asymmetry in these discharges was investigated using MGI valves in opposite sectors of the machine. The assimilated fraction was shown to be equal for both valves in Section 3.1 and thus the W_{rad} is expected to be approximately equal between the valves for a given gas type and quantity. It therefore follows that any difference measured in W_{rad} for the same injection is a measure of toroidal radiation asymmetry.

Figure 13 left presents W_{rad} inferred from the FSS analysis assuming no toroidal asymmetries. With the exception of one outlier at 1.05 MJ, comparable radiated energies are measured between the LFS (empty symbols) and HFS (filled symbols) injections for

a given Mix. Z and injection quantity. This implies the same W_{rad} was measured in the injection and toroidally opposite sectors and thus toroidal asymmetries are negligible in the mitigated discharges presented. Similar results have been reported on DIII-D with toroidal peaking factors of 1.2±0.1 during the TQ phase, implying a lower toroidal peaking factor over the entire disruption sequence [37].
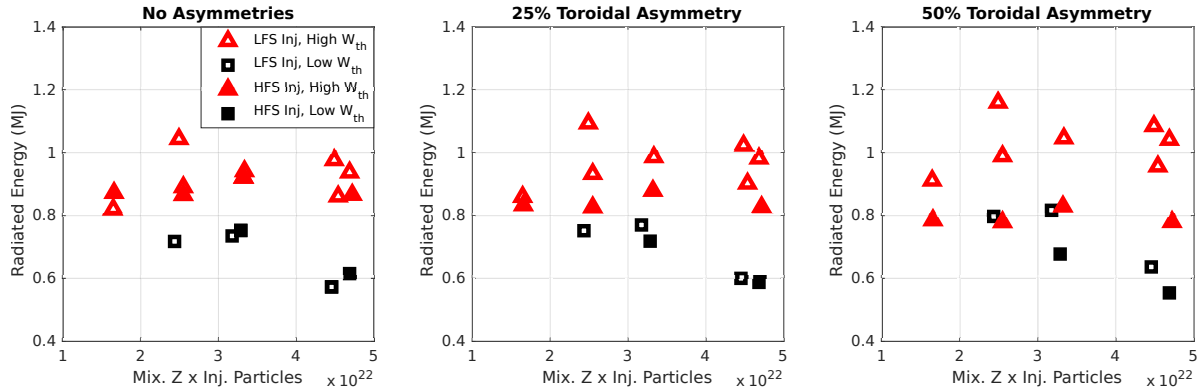

Figure 13. Radiated energy as a function of injected gas composition and quantity assuming 0%, 25% and 50% toroidal asymmetries from left to right.

The sensitivity of this methodology was investigated by artificially imposing 25% (Figure 13 middle) and 50% (Figure 13 right) toroidal asymmetries. A simple linear peaking profile was applied to calculate the W_{rad} presented. The calculated W_{rad} for the same injection (gas type and quantity) diverges as the asymmetry factor is increased and this could only occur if the same assimilated gas led to significantly different values of W_{rad}. Imposing a Gaussian peaking profile for the same analysis leads to stronger peaking in the injection sector and thus further divergence in W_{rad} between the two valves for the same injection. This sensitivity study indicates that a 50% toroidal asymmetry would produce a ~25% difference in W_{rad} for the same assimilated gas type and quantity. This result is implausible and supporting the finding that toroidal asymmetries are negligible in the mitigated discharges presented.

3.2.2. Uncertainties in Radiated Energy

Highly localised radiation emission and fast transient events can lead to significant uncertainties in W_{rad}. The following section presents an analysis aimed at quantifying uncertainties in the techniques used to infer W_{rad} and selecting the most appropriate one for the energy balance. Errors in the alignment of the cameras, capture angle, calibration and sensitivity variation between foils are assumed to be negligible relative to the errors in the inference techniques. The uncertainties for the AXUV diodes will not be discussed here as they are relatively calibrated using the bolometers and the impact of their photon energy dependent response is discussed in the relevant sections.

The single camera inference technique assumes constant emission along flux surfaces and this assumption is not appropriate for the highly localised radiation patterns in mitigated disruptions. Previous analyses using phantom reconstructions of standard

plasma emission profiles found a systematic underestimation of radiated power by up to 39% [33]. As previously discussed, localised radiation at the HFS leads to a significant overestimation during mitigated disruptions. Thus the uncertainties for the single camera technique are assumed to be significantly higher than those of the FSS and no FSS inversion methods and will not be further analysed here.

Three significant contributors to the uncertainty of total radiated power for the inversion techniques are the convergence of the inversion, radial position of high emission regions and the position or presence of negative emission regions. A direct comparison to determine the accuracy of a tomographic inversion is the reconstruction of radiation along each line of sight. The variation with respect to measured values can be used to estimate the quality of the match and convergence of the inversion. The reconstruction error is separated into positive and negative errors at each time point and the positive and negative integrals are presented separately in Figure 14. A positive error indicates W_{rad} is under-predicted and a negative error indicates overestimation. This analysis suggests that W_{rad} is systematically overestimated by the no FSS inversions and underestimated by the FSS inversions. The no FSS inversion overestimates by up to 21% compared to up to 17% under-prediction by the FSS inversions. There are certain time points where the no FSS technique underestimates the radiation and this is indicated by the positive errors in the integrals. There are no time points at which the FSS analysis provided a negative error.
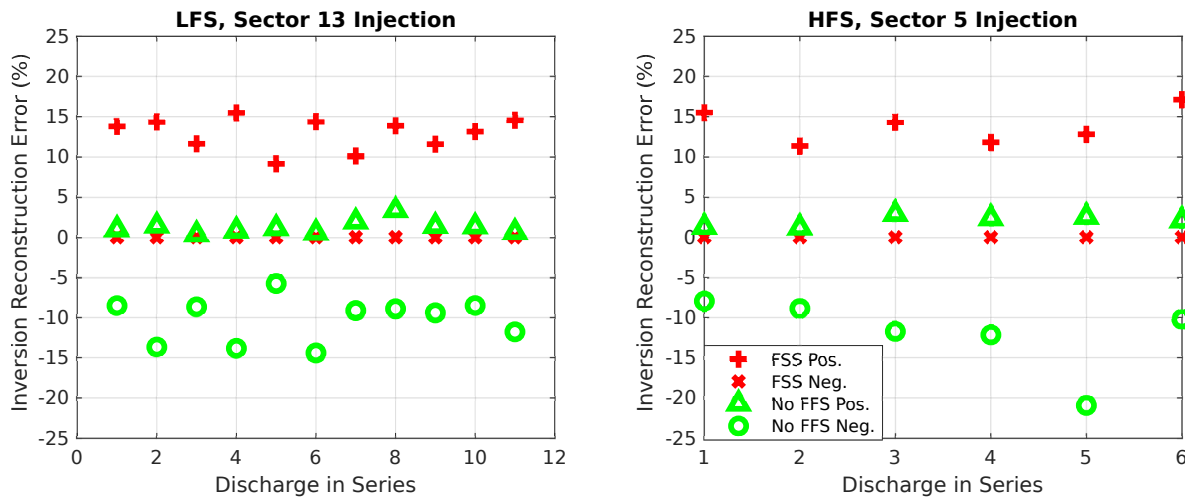

Figure 14. Error in reconstructed line of sight radiation for the bolometer inversion techniques. A positive error indicates under-prediction of W_{rad}.

The reconstructed location of strong emission zones can have a significant impact on the inference of W_{rad}. The most sensitive factor is the radial position as this can alter the volume of the radiating plasma. An example of this is shown in Figure 11 where the FSS method reconstructs a strong emission region close to the HFS wall and the no FSS method places it further inside the plasma. The difference in radial location from $\sim 1.20\,\mathrm{m}$ to $\sim 1.45\,\mathrm{m}$ results in a variation of radiating volume of $\sim 20\%$. This trend is

Table 2. Uncertainties in W_{rad} inferred from bolometric inversions.

Uncertainty Source	FSS	No FSS
Inversion convergence (maximum)	+17/0%	+4/-21%
Localisation of high radiation zones	+20/-0%	+0/-20%
Location of negative values	+0/-7%	N/A
Total	+37/-7%	+4/-41%

repeated in all inversions studied and partially accounts for higher W_{rad} inferred with the no FSS technique. The uncertainty from radial location is therefore estimated to be +20% for the FSS method and -20% for the no FSS method.

The FSS inversion technique permits negative emission regions to reduce computation time. They are included in the calculation of total radiated power but this been shown to produce no significant errors during standard operation [31]. However, in mitigated plasmas with highly poloidally asymmetric emission profiles, the location of negative emission regions can contribute to errors in the total radiated power. The absolute values of negative emission were found to be typically one third of the positive emission when the radiated power was above 50 MW and the location was generally observed to be at the LFS. Consequently, a total W_{rad} uncertainty of -7% was estimated from the radial emission location analysis.

A summary of the uncertainties produced by the factors discussed are presented in Table 2. The individually calculated errors from the inversion reconstruction were coupled with the estimated uncertainties due to emission location to provide the values presented in Figure 12. Most of the uncertainty range is overlapped by both inversion techniques for LFS injection indicating the possibility of using the two techniques together to better constrain W_{rad}. The larger discrepancy when using the HFS valve indicates the no FSS method is not well suited to localised emission at the HFS and this is assumed to be the reason for the unrealistically high total radiated energies computed (over 90% of the total pre-disruption energy). Therefore, the FSS inversion will be used for the remaining analysis presented in this study whilst noting that these inferences are likely under predicting the total W_{rad}.

4. Energy Balance

The energy balance methodology applied in this study is based on the model presented in Lehnen 2013 [23]. The two unknowns in the disruption energy balance are the total W_{rad} and W_{coupled}. Section 3.2 outlined the process used to constrain W_{rad} with the bolometers leaving W_{coupled} as the remaining unknown. This section presents a novel method to estimate W_{coupled} from diagnostic measurements on AUG and provide a comparison for simulations of these discharges currently being carried out to calculate W_{coupled}.

The high temporal resolution AXUV diodes were utilised to estimate the fraction of total radiation emitted prior to the start of the CQ, determined by the spike in plasma

current. These fractions were multiplied by the W_{rad} measured over the entire disruption to estimate W_{rad} prior to and during the CQ. The AXUV array in the toroidally opposite sector was used instead of the array in the injection sector to minimise the influence of the high relative sensitivity to visible photons (see Figure 4). As the sector 13 AXUV system was not available during the session with HFS injection, this analysis could only be applied to the LFS injection discharges. The results of this analysis are presented as fractions of W_{th} and W_{mag} radiated in Figure 15.
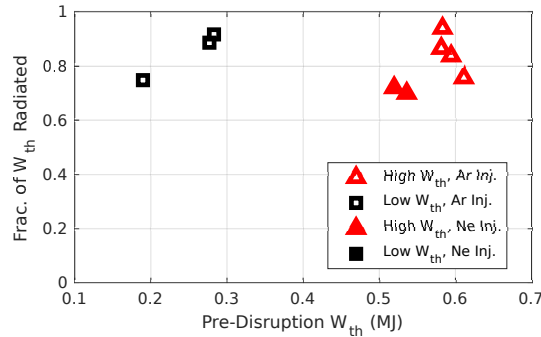

Figure 15. Fraction of W_{th} radiated as a function of pre-disruption W_{th}.

Radiated W_{th} fractions of 0.7-0.95 were inferred for the bulk of the discharges. Argon injections produced ∼10% higher radiated fractions at high pre-disruption W_{th} that is likely due to the higher radiation efficiency of argon and/or the relative spectral response of the diodes for the two gases. No decrease in fraction of radiated W_{th} was observed with increasing pre-disruption W_{th}.

The fraction of W_{th} that is not radiated is expected to be deposited on the divertor during the TQ. A comparison between W_{th} deposited and all three IR cameras was not possible as injected impurities resulted in significant radiation being recorded that masked the real target temperature. The camera observing two optimised tiles on the outer divertor was able to produce usable images at 1.5 ms temporal resolution. Figure 16 shows three sequential frames from this camera showing the strike point at gas arrival (top), beginning of the TQ (mid) and during the CQ at approximately 600 kA (bottom) for the reference discharge #35653. The strike point on both tiles can be clearly located by the localised higher temperature. The increase in baseline temperature in the second image is ascribed to plasma radiation and their reflections.

Figure 17 presents the maximum change in average tile surface temperature (dT) for a given W_{th} during the disruption. It should be noted that the relatively low temporal resolution can result in the dT being measured up to 1.5 ms after the end of the TQ, which can lead to an underestimation of TQ dT. An increase in dT was observed with increasing W_{th} deposited for argon injections and the neon injection disruptions produced a relatively lower dT for their estimated deposited W_{th}.

This is attributed to the variation in spectral mission of the two gases coupled to strong AXUV spectral sensitivity, influencing the radiated W_{th} estimate. The extrapolated dT with no deposited energy is 100 K and this offset is attributed to
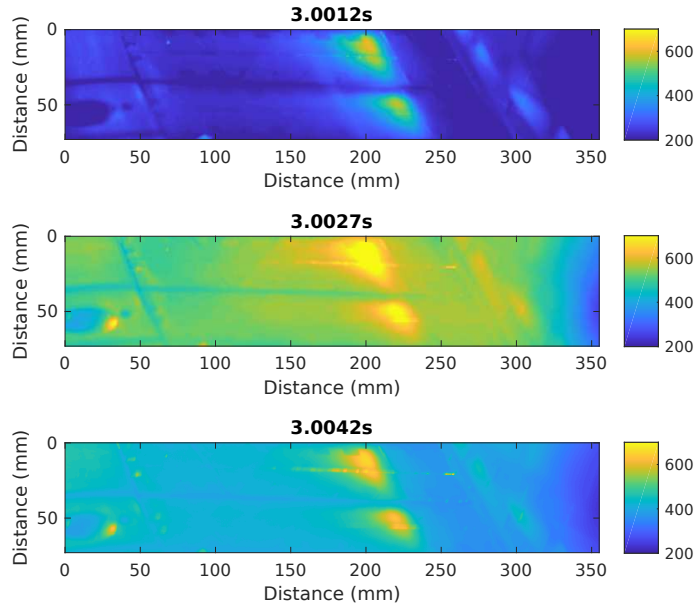
Figure 16. Left - IR images of the outer divertor target tiles during the reference discharge (#35653) at gas arrival (top), beginning of the TQ (mid) and during the CQ at approximately 600 kA (bottom).

a combination of background plasma emission and reflections being recorded on the camera.
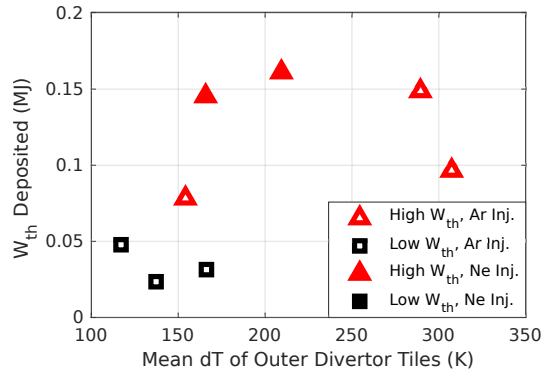

Figure 17. Maximum change of average outer divertor target temperature during the disruption as a function of deposited W_{th}.

The fraction of radiated W_{mag} is presented in Figure 18 and was approximately constant at 0.4 for all CQ times with no difference in radiated W_{mag} fraction observed between the two injection gases. The balance between radiated, deposited and coupled W_{mag} was explored in Lehnen [23]. It was shown that MGI mitigated plasmas without a vertical displacement event resulted in short CQ times normalised to the plasma cross-section area (2-10 ms/m^2). The time scales required for Ohmic heating of the plasma and heat conduction to the wall during the CQ were of the order of (100 ms/m^2) and only occurred in unmitigated disruptions with the ITER like wall. The plasma surface area was ~1.1m^2 for all the discharges presented and the normalized CQ times are

3.2-6.4 ms/m^2. These short normalized CQ times imply they are strongly radiation dominated and any W_{mag} not radiated can be assumed to be coupled to the vessel structure and coils.
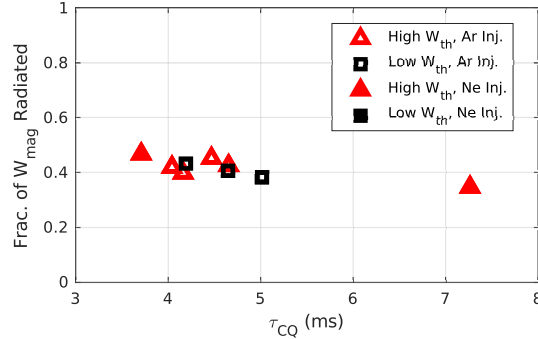

Figure 18. Fraction of W_{mag} radiated as a function τ_{CQ}.

The discharges produced an almost constant radiated W_{mag} fraction of ~0.4 and thus a W_{coupled} fraction of ~0.6. This is comparable with an almost constant W_{coupled} fraction of 0.5 reported across a range of discharges on DIII-D and over 0.6 on JET [36, 23]. Halo current (I_{halo}) measurements from the inner divertor shunt resistor and eight strain gauges mounted on the vertical tokamak support columns were used to validate the constant inferred W_{coupled}. Figure 19 presents times traces for both of these diagnostics. The sum of all eight strain gauges provided an estimate of the net vertical force the ignored distortion and twisting forces. The signal was zeroed at the time just before the disruption to measure only the vertical forces caused by the disruption by compensating for the strain measured from the load of the vessel itself.

Increases in I_{halo} were observed during the CQ and the peak value was comparable for most discharges. The I_{halo} profile for the final discharge in the LFS injection dataset, indicated by the dashed magenta line, is relatively offset in time that is attributed to the longer CQ time. Similarly, the last two discharges in the HFS injection dataset are also relatively offset in time. These two discharges produced relatively higher peak I_{halo} that is attributed to a vertical movement of the plasma. Consequently, the highest vertical forces were measured for these two discharges.

4.1. Radiated Energy Fraction

The W_{rad} from FSS inversions with inferred W_{coupled} from the AXUV diodes was used to calculate f_{rad} and f_{th} as described in Equations 1 and 2. A value of 0.60 was used for the W_{coupled} fraction for discharges where the AXUV diodes failed to provide a result. The calculated values of f_{rad} are presented in Figure 20, with the empty red circle markers indicating LFS injection and filled red circle markers for HFS injection. Values of f_{rad} ranging from 0.8 to 1.0 were calculated with no reduction in f_{rad} as f_{th} increased. The error bars presented represent solely the radiated energy uncertainty and do no include uncertainties in W_{coupled}.
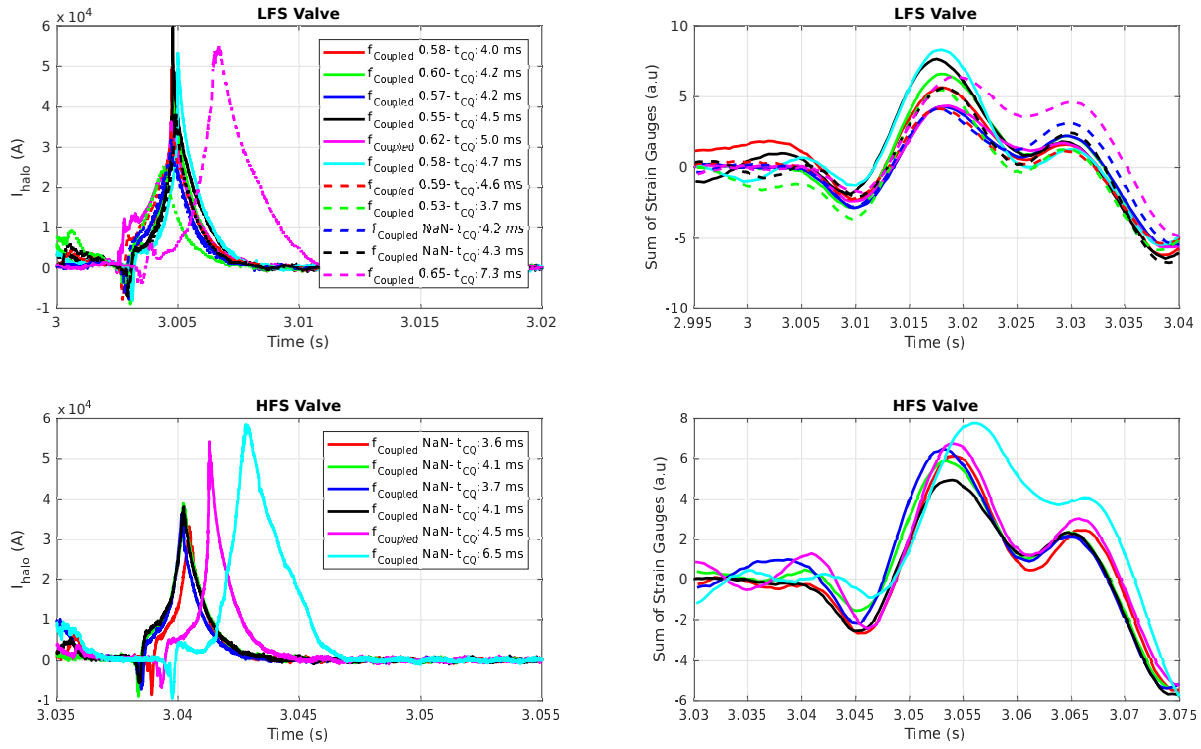
Figure 19. Left - I_{halo} measured at the inner divertor shunt for all discharges. Right - Sum of all eight strain gauges mounted on the vertical vessel support columns.
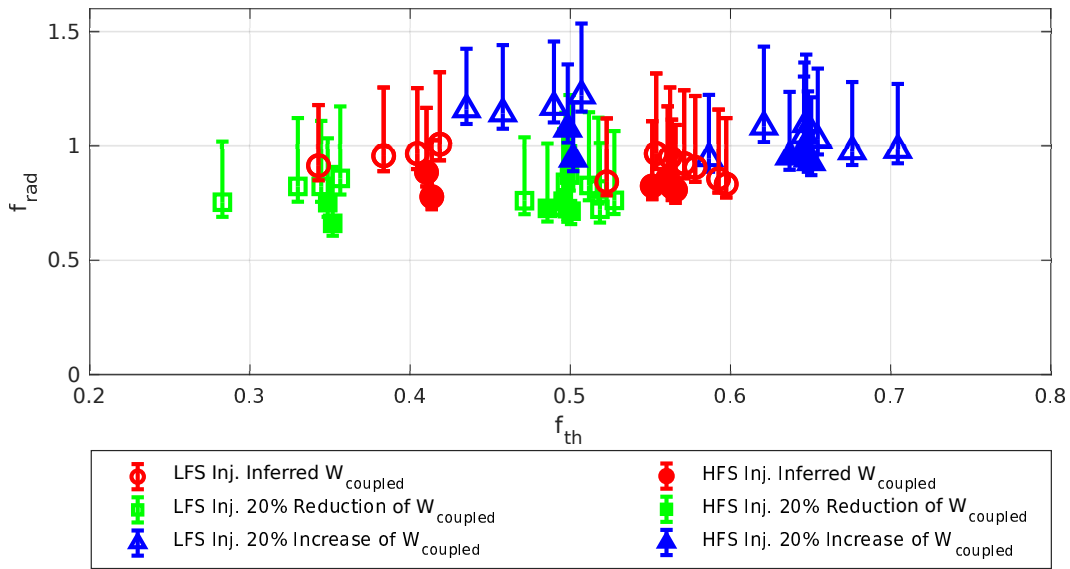

Figure 20. Computed f_{rad} as a function of f_{th} for LFS (empty markers) and HFS (filled markers) injection. Red circle markers - f_{rad} computed with inferred W_{coupled} from the AXUV diodes. Blue triangle and green square markers - f_{rad} computed with an artificial 20% increase and decrease in W_{coupled} respectively.

The photon energy dependent sensitivity of the AXUV diodes leads to uncertainties in the estimation of W_{rad} prior to and during the CQ. For example, it is shown in Figure 4 that the diodes have higher sensitivity to visible photons than UV photons. If more visible light is emitted prior to the CQ, this would alter the ratio and lead to an underestimation of CQ W_{rad} and an overestimation of W_{coupled}. It is difficult to constrain this uncertainty without fast spectrally resolved measurements but the impact of such an error can be explored through the variation of W_{mag} radiated or coupled. A 20% overestimation of radiated W_{mag}, due to relatively higher sensitivity of the diodes during the CQ, would result in a 20% underestimation of W_{coupled}. The impact a $\pm20\%$ error in W_{coupled} on f_{rad} is presented with the blue triangle and green square markers in Figure 20.

An underestimation of W_{rad} during the CQ would lead to an overestimation of W_{coupled}. A 20% increase of W_{coupled} results in f_{rad} values over one and this is non-physical (over 100% of W_{th} radiated). This clearly indicates that W_{rad} during the CQ is not being significantly underestimated. A 20% decrease of W_{coupled}, due to a potential 20% overestimation of W_{rad} during the CQ, leads to a decrease in f_{rad} but does not alter the constant f_{rad} found for a range of f_{th} values.

An additional constraint of the radiation dominated CQ model applied is the convergence of f_{rad} to one as f_{th} approaches zero [23]. As f_{th} approaches zero, the total plasma energy is effectively W_{mag}, which can only be radiated or coupled and thus f_{rad} must equal one. The almost constant f_{rad} value of one with varying f_{th} implies these discharges are well mitigated and the trend meets the constraint discussed. The size of the error bars on the radiated energy measurement do not allow for further convergence on W_{coupled}, however, it can be concluded that the W_{coupled} is likely between 48-60% of W_{mag}. Within the range of W_{coupled} explored, no variation of f_{rad} as a function of f_{th} was found.

5. Conclusions

This study has produced a disruption mitigation dataset targeting a constant plasma scenario with varying auxiliary power. Scans of two injection quantities with 90% deuterium and 10% neon or argon gas mixtures were performed at two nominal values of f_{th} and with two MGI valves at different toroidal and poloidal locations. This study investigated MGI assimilation, influence of bolometer inversion techniques of fast evolving radiation patterns, estimates of W_{coupled}, radiation asymmetries and the disruption power balance that can be achieved on AUG with current diagnostics.

Three techniques to infer W_{rad} using bolometers showed variations of up to a factor of two. These differences were attributed to convergence limitations and radial positions of strong emission locations. This highlight the large uncertainty in W_{rad} measurements with the current techniques and suggests this uncertainty could be reduced through emission location inferences from additional diagnostics. The FSS method was selected as the most reliable for emission profiles strongly peaked at the HFS and used to

investigate toroidal asymmetries. The fueling efficiency was found to be equal for the two valves. The CQ times and W_{rad} measured in the injection sector and toroidally opposite sector were independent of the valve used. Thus, asymmetries were estimated to be negligible for these discharges.

The AXUV diodes cross-calibrated with the bolometers were used to estimate the fractions of W_{th} and W_{mag} radiated. The difference between the pre-disruption W_{th} and W_{rad} before the end of the TQ was assumed to be deposited on the targets. The radiated thermal energy fraction was found to be 75-95% and the deposited energy correlated qualitatively with changes in tile surface temperatures. The inferred fraction of W_{mag} coupled was ~ 0.6 and approximately constant compared to τ_{CQ}. This result was supported by the halo currents measured at the inner divertor and the vertical vessel forces.

The final energy balance produced f_{rad} values between 0.8 and 1.0 with no reduction in f_{rad} as f_{th} increased. The impact of an error in the inferred $W_{coupled}$ was explored via artificial variation of $W_{coupled}$ by $\pm 20\%$. An increase in $W_{coupled}$ produced non-physical results (over 100% of W_{th} radiated before the CQ). A 20% decrease in $W_{coupled}$ produced plausible results and was estimated to be close to the lower limit of $W_{coupled}$ for these discharges. This analysis suggests $W_{coupled}$ for these discharges is likely between 48-60%. Variations in $W_{coupled}$ within this range did not alter the almost constant f_{rad} as a function of f_{th}.

6. Acknowledgements

7. Bibliography

[1] Lehnen, M., *et al* 2009 *J. Nucl. Mater.* **740** 390–391
[2] Federici, G., *et al* 2001 *J. Nucl. Mater.* **290** 260-265
[3] Putvinski, S., *et al* in Fusion Energy 2010 (Proc. 23rd Int. Conf. Daejeon, 2010) (Vienna: IAEA) CD-ROM file [ITR-1-6] and http://wwwnaweb.iaea.org/napc/physics/FEC/FEC2010/index.htm
[4] Lehnen, M., *et al* 2011 *Nucl. Fusion* **51.12** 123010.
[5] Arnoux, G., *et al* 2011 *J. Nucl. Mater.* **415** S817
[6] Whyte, D.G., *et al* 2007 *J. Nucl. Mater.* 363–365 1160–7
[7] Pautasso, G., *et al* 2009 *Plasma Phys. Control Fusion* **51** 124056
[8] Hollmann, E.M., *et al* 2008 *Nucl. Fusion* **48** 115007
[9] Bakhtiari, M., *et al* 2005 *Nucl. Fusion* **45** 318–25
[10] Thornton, A.J., *et al* 2011 *J. Nucl. Mater.* S836 415
[11] Luo, Y. H., *et al* 2014 *Rev. Sci. Instruments* **85.8**: 083504

[12] Dong, Y. B., *et al* 2014 *No. NIFS-PROC–97*

[13] Commaux, N., *et al* 2010 *Nucl. Fusion* 50 112001

[14] Baylor, L.R., *et al* 2019, *APS* YP10-061

[15] Park, S.H., *et al* 2020 *Fusion Eng. and Design* 154 111535

[16] Li, Y., *et al* 2018 *Rev. Sci. Instruments* **89.10**: 10K116

[17] Xu, H. B., *et al* 2019 *Fusion Science and Technology* **75.2**:98-103

[18] Hollmann, E.M., *et al* 2015 *Phys. Plasmas* 22 021802

[19] Commaux, N., *et al* 2016 *Nucl. Fusion* **56.4** 046007

[20] Lehnen, M., *et al* 2015 *J. Nucl. Mater.* 39-48 463

[21] Jachmich, S., *et al* 2016 *The 22nd PSI-conference*

[22] Joffrin, E., *et al* "Disruption studies in the JET metallic wall". Preprint: 2016 IAEA Fusion Energy Conf, Kyoto [EX/9-1]

[23] Lehnen, M., *et al* 2013 *Nucl. Fusion* **53** 093007

[24] Bernert, M., *et al* 2014 *Rev. of Sci. Instruments* **53.3** 104003

[25] Shiraki, D., *et al* 2018 *APS* DPPN11115S

[26] Neu, R., *et al* 2007 *Plasma Phys. Control. Fusion* **49** B59

[27] Meyer, H., 2019 *Nucl. Fusion* **59** 112014

[28] Pautasso, G., *et al* 2015 *Nucl. Fusion* **55.3** 033015

[29] Pautasso, G., *et al* in Fusion Energy 2008 (Proc. 22nd Int. Conf. Geneva, 2008) (Vienna: IAEA) CD-ROM file [EX/P9-1] and http://wwwnaweb.iaea.org/napc/physics/FEC/FEC2008/html/index.htm

[30] Meister, H., 2013 *Rev. of Sci. Instruments* **84** 123501

[31] Fuchs, J.C., *et al* 1994 *Proc. of 21st EPS*

[32] David, P., *et al* 2017 *Rev. of Sci. Instruments* **88.11** 113507

[33] Gloggler, S., 2018 *Masters Thesis*, Max Planck Institute for Plasma Physics, Garching, Germany

[34] Odstrcil, T., *et al* 2016 *Rev. of Sci. Instruments* **87.12** 123505

[35] Bernert, M., 2010 *Masters Thesis*,Max Planck Institute for Plasma Physics, Garching, Germany

[36] Shiraki, D., *et al* 2018 *60th APS* http://meetings.aps.org/link/BAPS.2018.DPP.NP11.115

[37] Shiraki, D., *et al* 2015 *Nucl. Fusion* **55.7** 073029